Journal of Materials Chemistry A

PAPER

View Article Online
View Journal

Cite this: DOI: 10.1039/c9ta08378b

Hexagonal perovskite related oxide ion conductor $Ba_3NbMoO_{8.5}$: phase transition, temperature evolution of the local structure and properties†

Matthew S. Chambers,[ab] Kirstie S. McCombie,[c] Josie E. Auckett,[a] Abbie C. McLaughlin,[c] John T. S. Irvine,[d] Philip A. Chater,[b] John S. O. Evans*[a] and Ivana Radosavljevic Evans*[a]

$Ba_3NbMoO_{8.5}$ has recently been demonstrated to exhibit competitive oxide ion conductivity and to be stable under reducing conditions, making it an excellent potential electrolyte for solid oxide fuel cells. We report here the first investigation of the local structure in $Ba_3NbMoO_{8.5}$, carried out using variable-temperature neutron total scattering and pair distribution function (PDF) analysis. This work reveals a significant degree of disorder in the material, even at ambient conditions, in both the cation and the anion arrangements and suggests the prevalence of the five-fold Nb/Mo coordination. In addition, high resolution powder X-ray diffraction data indicate that the temperature-dependent structural changes in $Ba_3NbMoO_{8.5}$ are due to a first order phase transition, and reveal a previously unreported effect of thermal history on the room-temperature form of the material. PDF modelling shows that $Ba_3NbMoO_{8.5}$ has an essentially continuous oxygen distribution in the *ab* plane at 600 °C which leads to its high oxide-ion conductivity.

Received 1st August 2019
Accepted 25th October 2019

DOI: 10.1039/c9ta08378b

rsc.li/materials-a

Introduction

Research into oxide ion conductors is driven by their existing and potential applications in oxygen sensors and pumps,[1] separation membranes,[2,3] and as electrolytes in solid oxide fuel cells (SOFCs).[4–6] High oxide ion conductivities have been identified in a number of structural families, including fluorites (and derivatives), simple perovskites, apatites and rare-earth molybdates. However, the discovery of this useful and exploitable property in a new structure type is significant as it may provide routes to better-performing materials.

One such recent case is the discovery of high oxide ion conductivity in $Ba_3NbMoO_{8.5}$ and the related $Ba_3Nb_{1-y}(Mo_{1-x}W_x)_{1+y}O_{8.5+1/2y}$ ($0 \leq x \leq 1$, $-0.3 \leq y \leq 0.2$) phases.[7–11] The NbMo member shows a bulk conductivity of 2.2×10^{-3} S cm^{-1} at 600 °C with a reduction in activation energy from 1.21 to 0.71 eV around 500 °C. Concentration cell measurements showed conductivity was predominantly due to oxide ions at oxygen partial pressures from 10^{-20} to 1 atm (oxygen transport numbers 0.97–0.99 in air/O_2 and 0.90–0.94 in air/5% H_2 in Ar).[9] These materials can be described as adopting a cation- and anion-deficient derivative of the 9R perovskite structure $A_3B_3O_9$ (A =

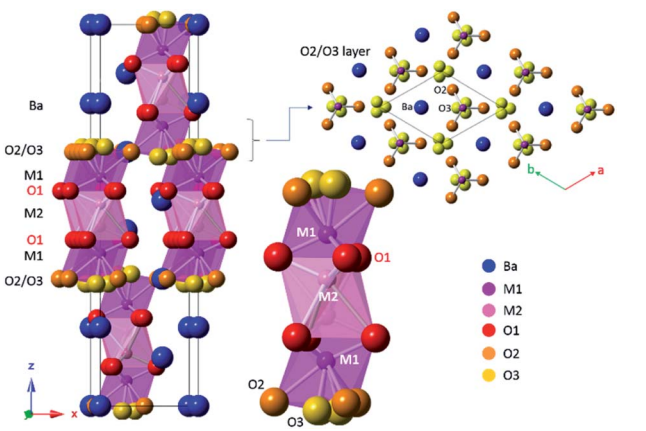

Fig. 1 The crystal structure of $Ba_3NbMoO_{8.5}$. Blue spheres represent Ba atoms. Magenta and pink polyhedra, respectively, are centred on the M1 and M2 sites, over which Mo and Nb are disordered. Red spheres are the fully occupied O1 sites, while orange and yellow spheres depict the partially occupied O2 and O3 sites, respectively. (Centre) Close up of the M1–M2–M1 "trimers" of face-sharing coordination polyhedra. (Top right) A section of the structure viewed down the *c* axis showing a layer containing partially occupied O2/O3 sites and the M1 atoms above this layer. View corresponds to Fig. 6c and d.

[a]Department of Chemistry, Durham University, South Road, Durham, DH1 3LE, UK. E-mail: ivana.radosavljevic@durham.ac.uk

[b]Diamond Light Source, Diamond House, Harwell Science and Innovation Campus, Didcot, OX11 0DE, UK

[c]The Chemistry Department, University of Aberdeen, Meston Walk, Aberdeen, AB24 3UE, UK

[d]School of Chemistry, University of St Andrews, St Andrews, Fife, KY16 9ST, UK

† Electronic supplementary information (ESI) available. See DOI: 10.1039/c9ta08378b

alkaline earths, B = transition metal *etc.*), where 1/3 vacancies are distributed across the B sites (Fig. 1). The structure was initially described as containing only (Nb/Mo)O_4 tetrahedra and (Nb/Mo)O_6 octahedra,[9] and the degree of oxide ion conductivity was correlated with the changing ratio of (Nb/Mo)O_4 tetrahedra and (Nb/Mo)O_6 octahedra with increasing temperature.[7,10] The more recent, and so far the only, single crystal diffraction study of these materials, has demonstrated that the structure is more complex, with significant crystallographic disorder in both the cation and anion sublattices.[12] The oxygen sub-stoichiometry relative to the 9R perovskite $A_3B_3O_9$ structure results in a distribution of (Nb/Mo)O_n polyhedra at the terminating ends of the face-sharing stacks, suggesting that the tetrahedral/octahedral dichotomy used in earlier descriptions of the structure as a 9R/palmierite intergrowth is incomplete. Importantly, the single crystal study[12] indicated that the presence of five-coordinate (Nb/Mo)O_5 is not only possible, but very likely, thus resolving the problem with the proposed changing numbers of (Nb/Mo)O_4 tetrahedra and (Nb/Mo)O_6 octahedra in the structure (without a concurrent change of the composition of the material or a dramatic phase transition altering connectivity), which had not been addressed in the previous literature.

To fully understand the bulk properties of materials such as these it is crucial to understand their local structure as well as average crystallographic structure. One experimental technique that can provide this understanding in functional oxides is neutron total scattering coupled with pair distribution function (PDF) analysis.[13–15] We report here the first investigation of the local structure in $Ba_3NbMoO_{8.5}$ by variable-temperature neutron total scattering and PDF analysis. This work reveals a significant degree of structural disorder in both the cation and the anion arrangements, and the prevalence of the five-fold Nb/Mo coordination. We also report variable-temperature high resolution powder X-ray diffraction studies which reveal a first-order phase transition in $Ba_3NbMoO_{8.5}$. In addition, high resolution powder X-ray diffraction studies demonstrate that the room-temperature form of the material depends on the detail on the thermal history. Jointly, this multi-length scale structural study enables us to propose new structure–property relationships in $Ba_3NbMoO_{8.5}$ and related materials.

Experimental

Synthesis

$Ba_3NbMoO_{8.5}$ was synthesised by grinding stoichiometric amounts of $BaCO_3$ (Aldrich, 99.98%), MoO_3 (Aldrich, 99.5+%) and Nb_2O_5 (Aldrich, 99.99%) together and pressing them into ten 1 g pellets. The pellets were calcined in an alumina crucible at 900 °C for 10 h. The pellets were reground, repelletised and heated at 1200 °C for 48 h and cooled to room temperature at a rate of 5 °C min^{-1}. This was repeated (typically 3–4 times) until a phase-pure product (free of $BaMoO_4$) was obtained, as determined by powder X-ray diffraction. Once a phase-pure sample was obtained, the pellets (typically around 90–95% theoretical density) were ground together to make one sample. Thermogravimetric analysis was performed on the as-made sample with a Mettler Toledo TGA 2 coupled with a Hiden Quadrupole Mass Spectrometer in air. The sample was heated from 30 °C to 600 °C at a rate of 5 °C min^{-1}. Solid state ^{1}H NMR spectra were recorded on a 400 MHz Bruker Avance III HD spectrometer with a delay time of 60 s. Samples were packed in a 4 mm rotor and spun at 10 kHz. Tetramethylsilane was used as a reference.

Neutron total scattering

Approximately 6.7 g of $Ba_3NbMoO_{8.5}$ powder was loaded into an 8 mm diameter V can, filled to a depth of 5.1 cm. Cans were sealed in air then heated in a furnace evacuated to $\sim 10^{-5}$ mbar. Neutron total scattering data were collected on the POLARIS instrument at the ISIS Neutron and Muon Source. PDF-quality data were obtained at room temperature and 600 °C, by collecting eight 1 h datasets at each temperature, which were subsequently merged. Rietveld-quality data were obtained using ten minute data collections from 50–575 °C in 25 °C intervals. To obtain Bragg scattering data, the data were processed using routines within Mantid software.[16] Rietveld refinements were performed against the room temperature data by refining the cell parameters, atomic coordinates, the site occupancies of the Mo, Nb and O atoms, isotropic atomic displacement parameters (ADPs) and peak shape parameters. The Mo and Nb occupancies and ADPs on each site were equated due to the relatively small difference in neutron scattering lengths (b_{Mo} = 6.715 fm; b_{Nb} = 7.054 fm). Data collected from three detector banks were used: bank 3 ($2\theta = 52.2461°$), bank 4 ($2\theta = 91.5081°$) and bank 5 ($2\theta = 146.942°$). The final model obtained at room temperature was used as the starting point for the analysis of the high temperature data. All Rietveld analyses were performed using TOPAS Academic.[17,18]

For total scattering analysis, PDF-quality data were processed using GudrunN version 5 to produce $S(Q)$ data,[19] which were further processed with the STOG software to produce $G(r)$ and $F(Q)$ files. The $G(r)$ data were produced using $Q_{max} = 35$ Å^{-1} and a Lorch correction was applied to both room temperature and 600 °C data to remove Fourier ripples resulting from Fourier transform over a limited Q_{max}. A low-r Fourier filter was applied with a cut-off of 1.6 Å.

Total scattering analysis was performed using TOPAS v6 for small-box refinements,[20] where the $G(r)$ were converted into $D(r)$ data normalised by the sum of the scattering from all pairs according to standard formalisms.[21] Configurations for RMCProfile[22] big-box refinements were created from Rietveld-refined average models, but with M2 and O3 sites (Fig. 1) initially placed on an adjacent special position for convenience. For the majority of the analysis, 8 × 8 × 4 supercells (~47 × 47 × 84 Å; $\alpha = \beta = 90°$, $\gamma = 120°$) were used which contained a total of 10 368 atoms. An additional 2688 vacancy sites were included to model the expected partial occupancy of M- and O2/O3-derived positions. An initial model-only site swapping run was performed in RMCProfile to produce starting configurations obeying chemically-sensible local bonding and avoiding unreasonable local environments. To investigate M1/M2 site distributions, different starting models were tested either with M1 sites fully occupied or with M1 and M2 sites populated to mimic the Rietveld-derived occupancies as closely as possible for the box size used. This process produces a mixture of initial

occupation patterns of the 3 available M sites within each M1–M2–M1 trimer (Fig. 1), and the occupation patterns generated matched those expected on statistical grounds. During fitting, the Bragg: $D(r) : F(q)$ data were weighted at 1 : 2 : 6, minimum distance restraints were applied to prevent unreasonably short atomic approaches, and weak bond valence restraints were applied to maintain chemically plausible structures, particularly in the early stages of fitting. A typical RMCProfile run converged in about 10^7 moves of atomic shifts and site swapping (performed in a 4 : 1 ratio). 8 different starting configurations were fitted and the resulting atomic models averaged in the data analysis. The cloud plot of Fig. 4 was produced using an equivalent procedure with a simulation box transformed from the average structure to give an approximately tetragonal metric in the *ab* plane ($\sim 41.5 \times 41.1 \times 84.4$ Å; $\alpha = \beta = \gamma = 90°$) containing 9072 atoms. "Cloud plot" figures were produced using the VESTA software package.[23]

Synchrotron X-ray powder diffraction

High resolution synchrotron powder X-ray diffraction data were collected on the I11 beamline at Diamond Light Source (DLS). The data were collected using a wavelength of $\lambda = 0.824681$ Å and the high resolution multi-analysing crystal (MAC) detector. The sample was loaded into 0.3 mm diameter quartz capillary. A hot air blower was used to control the temperature. The temperature was calibrated using an Al_2O_3/Si standard. Data were collected for 10 minutes at each temperature, with temperature change and equilibration taking 7 minutes. The overall effective heating and cooling rate during the experiment was ~ 1.8 K min^{-1}.

Results and discussion

Average structure of $Ba_3NbMoO_{8.5}$ as a function of temperature

The average structure of $Ba_3NbMoO_{8.5}$ determined from powder neutron diffraction data has been reported before,[9,10] so here we give only a short description emphasising the differences between this study and the previous literature. Our starting model included a split M2 cation position (Fig. 1), as found in the single crystal XRD study, and consistent with off-centring of the d^0 transition metal.[12] Fractional coordinates and isotropic ADPs were refined, with M1 and M2 ADPs equated. The M1 and M2 site occupancies refined to the expected total value of 2 M cations per formula unit (refined value 1.96(2)). Independently refining the fractional occupancies of the O2 and O3 sites resulted in a total O content of 8.52(2) and a fit with $R_{wp} = 3.332\%$. The same model was used for the 600 °C data analysis and gave a total O content of 8.42(2) and $R_{wp} = 3.832\%$. The crystallographic parameters of these models are presented in Tables S1 and S2 of the ESI† and the Rietveld plots are in Fig. S1 and S2.†

To gain further insight into changes in the average structure on heating, Rietveld refinement was performed against the 21 data sets collected between room temperature and 600 °C. Key results are plotted in Fig. S3 and S4 of the ESI.† There are four main conclusions from this analysis: (1) while the total Mo + Nb content per unit cell remains unchanged with temperature, we see a shift of cations from M2 to M1 sites starting at ~300 °C. (2) The change in M1/M2 occupancy is accompanied by an apparent decrease in the O2 occupancy and increase in O3. (3) The total oxygen content per formula shows a slight apparent decreases from 8.52(2) to 8.42(2) between room temperature and 600 °C. (4) Whilst a single phase model gives a good fit to the medium-resolution diffraction data at all temperatures, we see an unusual dependence of cell parameters on temperature; this is discussed in the context of a phase transition in the next section. Observations (1) and (2) are qualitatively similar to previous studies on this material.[8,11]

A small apparent decrease in oxygen content of $Ba_3NbMoO_{8.5}$ with temperature has also been reported recently by Yashima *et al.*,[24] who observed similar occupancy changes in their neutron powder diffraction experiments and a small mass loss by TGA. Our own TGA results (Fig. S5 in ESI†) show a small mass loss below 200 °C which we attribute to surface water, and a further mass loss of up to ~0.4% up to 600 °C. This would correspond to ~0.18 O per formula unit, but a combined TGA-MS experiment suggests H_2O is the primary species evolved. ^{1}H solid state NMR experiments (Fig. S6†) also reveal small but significant proton signals suggesting minor water uptake. A weak signal is observed at ~3 ppm even in samples heated to 600 °C, and a significantly stronger signal appears at ~5 ppm after holding samples at 75% relative humidity at room temperature for 5 days. Previously published impedance and concentration cell studies[8] on samples prepared in the same way as those studied here also give no indication of the significant electronic conductivity that would be expected if the level of oxygen loss implied by the refined occupancies occurred.

Rietveld refinements in which a soft restraint is applied to the total oxygen content give an essentially unchanging composition with temperature and only a marginal increase in R_{wp} values (largest change 0.001% for the 21 refinements; Fig. S3†). We also find significant correlation between O content and M1/M2 occupancies: if M2 occupancy is set to zero, an isotropic refinement gives a refined oxygen content of 8.50(3) at 600 °C. Simultaneous determination of accurate occupancies and ADPs from Rietveld refinement is known to be problematic, even from high quality neutron data such as this, and the precision of such results, as represented by the standard uncertainties from the least squares analysis, is typically an under-representation of the true error.[25] We also note that apparent composition changes of a similar magnitude occur in other disordered oxides as a function of temperature where there is no chemical reason to expect sample reduction.[26] Given the significant disorder in the local structure discussed below, it is likely that the apparent reduction in oxygen content when refining multiple site occupancies is an artefact of the isotropic oxygen ADPs inadequately describing the true average atomic density from these sites, resulting in an underrepresentation of the occupancy. We therefore conclude that, whilst we can't exclude the possibility of a small amount of oxygen loss, the majority of mass loss from our sample is due to water.

First order phase transition in $Ba_3NbMoO_{8.5}$

An inspection of the unit cell parameters of $Ba_3NbMoO_{8.5}$ (and $Ba_3NbWO_{8.5}$) in the literature reveals some disagreement between different reports. In addition, our work revealed different unit cell parameters for samples of $Ba_3NbMoO_{8.5}$ prepared in the same batch, which had undergone different thermal treatments. Moreover, some samples displayed splitting of certain powder diffraction peaks, with changeable relative intensities of the components.

We have therefore undertaken variable temperature high-resolution synchrotron X-ray powder diffraction experiments to investigate this behaviour. Diffraction patterns collected between room temperature and 600 °C on beamline I11 at Diamond Light Source are shown in Fig. 2. Several peaks show marked changes above ~150 °C on heating which indicate a significant structural change. At temperatures between 150 and 370 °C two phases are observed. This is the same temperature region where the neutron study showed unusual cell parameters changes and changes of the M1/M2 and O2/O3 site occupancies.

The temperature evolution of unit cell parameters, obtained by Rietveld fitting using two $Ba_3NbMoO_{8.5}$-like phases is shown in Fig. 2b–d. At the beginning of the experiment, a single phase is present (Fig. 2e). However, from ~150 °C, a second phase begins to form with a smaller a cell parameter (Fig. 2b) and a larger c cell parameter (Fig. 2c), with an overall smaller unit cell volume (Fig. 2d). The phase with the smaller a cell parameter gradually increases in abundance (Fig. 2e) until ~370 °C, where it becomes the sole phase present. On cooling to 330 °C no reverse transition was seen on the timescale of the experiment. Based on the Rietveld refinements discussed above and the local structural study discussed below, it seems likely that the high and low temperature phases differ in the distribution of M cations between M1 and M2. The redistribution of cations across these sites is likely to slow significantly at low temperature and lead to the observed dependence of structure on thermal history. The overall thermal expansion coefficients between 40 and 800 °C are $\alpha_a = 18.5 \times 10^{-6}$ K^{-1}, $\alpha_c = 17.9 \times 10^{-6}$ K^{-1}, $\alpha_V = 55.5 \times 10^{-6}$ K^{-1}.

Local structure of $Ba_3NbMoO_{8.5}$

Initial small-box fitting of the neutron PDF data collected at room temperature and 600 °C revealed that the average crystallographic structure is not sufficient to describe the local structure of $Ba_3NbMoO_{8.5}$ at either temperature (Fig. S7†), particularly in the low-r region. The data were therefore modelled using a big-box approach with 8 × 8 × 4 supercells containing a total of 13 506 sites to describe atom positions and

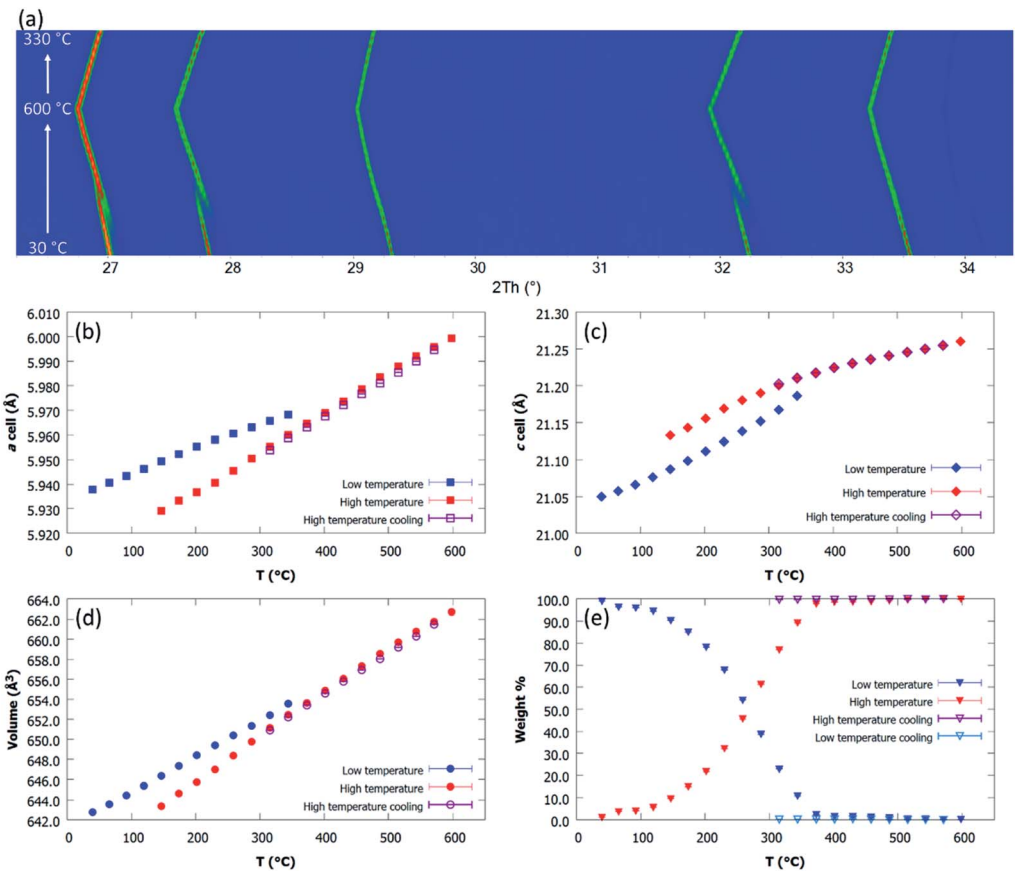

Fig. 2 Variable temperature synchrotron powder diffraction data recorded over approximately 8 hours: (a) surface plot of raw patterns on heating and cooling; (b–e) cell parameter and phase weight percentages from Rietveld refinement using two closely related $Ba_3NbMoO_{8.5}$ phases.

vacancies. Two distinct approaches were used to describe the starting M1/M2 site occupancies (M2 sites either populated based on Rietveld occupancy or empty) and 8 different starting configurations were used for each approach. Site swapping was used to generate O2/O3 starting configurations which obeyed sensible local bonding rules. An excellent fit was obtained to the $D(r)$, Bragg and $F(Q)$ data from each starting model, with the misfits in the small-box fitting eliminated. Fig. 3 shows representative fits at room temperature and 600 °C. Initial analysis showed that each configuration converged to an essentially equivalent model, and results from these models were therefore averaged in the data analysis that follows.

Fig. 4b shows the room temperature atomic density maps or "cloud plots" for M atoms only around the M1–M2–M1 trimers obtained by folding all supercell configurations into a single $P1$ unit cell. The three equivalent trimer clouds produced in this cell are visually very similar. We see a significant population of M2 cations located close to the positions indicated by single crystal studies. There appears to be a small distribution of M2 sites around the three fold axis. This could be caused by the neighbouring M1 site being 4, 5 or 6 coordinate. Classifying each of the 1536 M sites in each of the 8 configurations as M1 or M2 according to their nearest ideal site gave averages of 91.8% and 92.2% M1, 6.8% and 7.2% M2 (with 1.4% and 0.8% unassigned sites) for the RMCProfile runs that started from the different initial M1/M2 distribution models. The corresponding average site occupancies of 0.92 and 0.07 are in excellent agreement with the M1 and M2 fractional site occupancies of 0.913 and 0.087 obtained by Rietveld analysis. We note that initial configurations based on the Rietveld-derived M1 and M2 occupancies distributed the 2 × M cations per formula unit

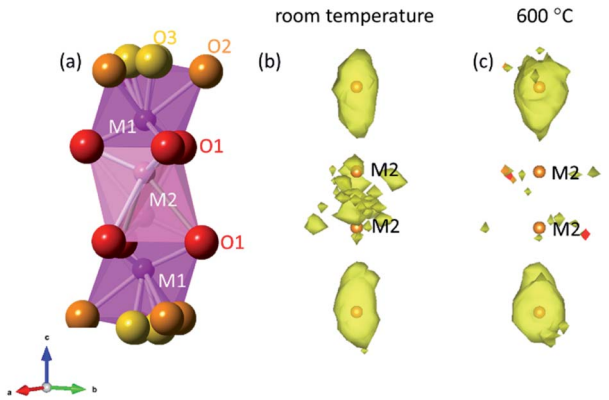

Fig. 4 Atomic density maps of M1 and M2 sites. The yellow surface encloses ~3500 atoms and is drawn at a contour level of 1.5 atoms per ~0.2 × 0.2 × 0.2 Å^3 voxel. The few isolated voxels represent a small number of atoms that have moved away from sensible positions during RMCProfile runs. Plots were derived from the ~tetragonal configurations and surfaces enclose ~99% of M atoms expected in this region.

statistically over the 3 possible sites of each trimer. As such, starting models contained a statistical mixture of trimers containing between 1 and 3 occupied metal sites. In the final configurations we see a preference for either M1–Vac–M1, M1–M2–Vac or Vac–M1–M2 groups, with the chemically less likely M1–M2–M1 pattern disfavoured (to maintain total M content this also implies double-vacancy patterns are disfavoured).

Fig. 4c shows the equivalent trimer map from the high temperature models. Consistent with the Rietveld analysis, these show that the M2 site is essentially unpopulated at high

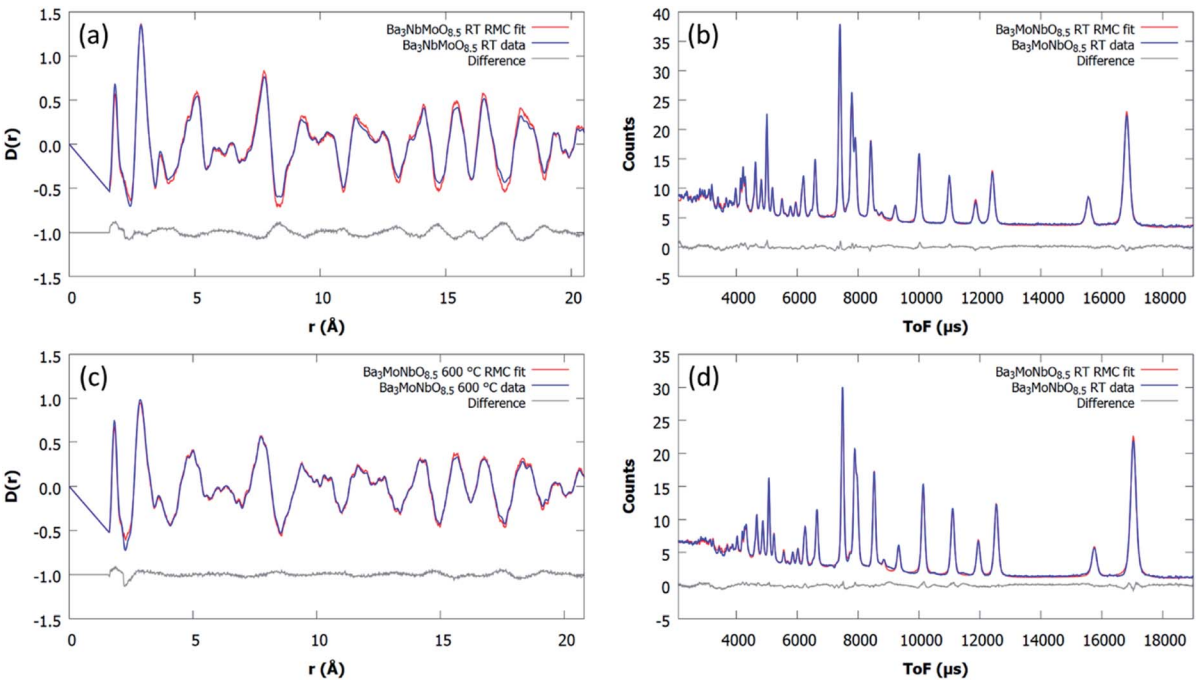

Fig. 3 Representative fits to $D(r)$ and Bragg data from RMC analysis of $Ba_3NbMoO_{8.5}$ at (a) and (b) room temperature and (c) and (d) 600 °C. In (b) and (d) counts are in arbitrary units.

temperature. All M atoms are tightly clustered around the M1 sites, though there is some elongation towards M2. The models now closely resemble an oxygen-deficient $Ba_3Re_2O_9$ structure. Assigning their atoms according to the nearest site gives 97.2% M1, 1.6% M2 (with 1.1% unassigned) for the various configurations. The corresponding average occupancies of 0.97 and 0.02 are again in excellent agreement with the M1 and M2 site occupancies of 0.970 and 0.030 obtained from Rietveld analysis.

Another important aspect of the $Ba_3NbMoO_{8.5}$ structure is the coordination number of the M cations. The variable (4, 5, and 6) coordination numbers of Mo^{6+} and Nb^{5+} have been shown to facilitate high oxide ion conductivity in several mixed metal molybdates and niobates.[27–30] In $Ba_3NbMoO_{8.5}$, however, the high oxide ion conductivity was initially linked to the ratio of the number of MO_4 tetrahedra to MO_6 octahedra,[7,8,10,11,31,32] while subsequent average structure determination implied that MO_5 polyhedra are highly likely to be present.[12] The coordination numbers of the M cations in our models were determined using a cut-off of 3.05 Å (based on the M–O distance histograms obtained from the RMCProfile modelling, Fig. S8† and the fact that this gave predominantly 6 coordinate M2 sites as expected; this cut off captures ~99% of the bond valence sum for each site), and are shown in Table 1. As expected from the fact that crystallographic models show full O1 occupancy, the M2 sites are overwhelmingly 6-coordinate. For M1, the coordination number 5 is prevalent at room temperature, with ~45% of M1 atoms adopting this environment. This suggests that the previous view of the structure in terms of only linked tetrahedra or octahedra is incomplete.

In the 600 °C model, the most common coordination number for M1 atoms is still CN = 5 (47%), as opposed to CN = 4 as previously suggested,[10] although the proportion of M1 atoms with CN = 4 has increased and those with CN = 6 decreased slightly compared to room temperature (Table 1).

A histogram of O–M1–O bond angles for each MO_n coordination number at each temperature is shown in Fig. 5. The 4- and 6-coordinate M1 sites show distributions close to those expected for regular tetrahedra and octahedra. In contrast, polyhedra with CN = 5 show a broad distribution of bond angles with two peaks at ~90° and ~170°, which suggests that

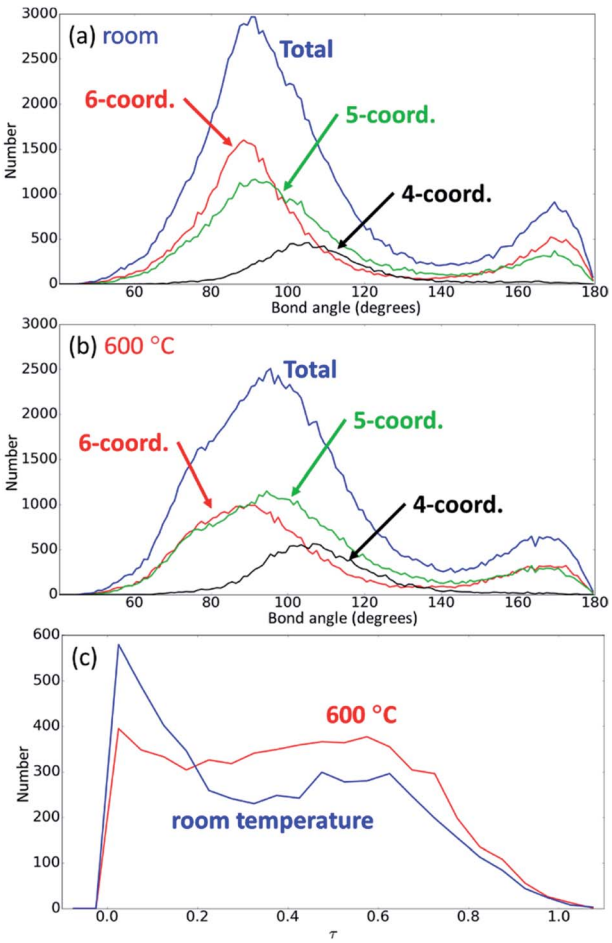

Fig. 5 The O–M1–O bond angle distributions at (a) room temperature and (b) 600 °C and (c) τ_5 plots at both temperatures.

square pyramids are the most common coordination geometry adopted. One way to quantify the 5-coordinate geometry is using the τ_5 descriptor[33] which is defined by $\frac{\beta - \alpha}{60^\circ}$, where β and α are the largest and second largest angles respectively, and varies from 0 to 1 between a square pyramid and trigonal bipyramid. Fig. 5c reveals a broad τ distribution at each temperature with a stronger preference for square pyramidal geometry at low temperature. As expected, the bond angle distributions broaden with increasing temperature.

While coordination number 5 is less common than 4 or 6 in structurally well-ordered oxides, it is found in a number of Nb^{5+} and Mo^{6+} containing compounds.[34] For example, five-fold coordination has been reported using a range of different techniques (single crystal and powder X-ray and neutron diffraction, IR and Raman spectroscopy, solid state NMR, computational methods).[27–30,35–37] Oxide ion conductors and other materials with oxide ion mobility are also more likely to exhibit less regular coordination environments. In $Ba_3NbMoO_{8.5}$, the five-fold coordination arises primarily due to the disorder and high level of vacancies in the oxide ion sublattice that are discussed here and in previous reports.[12]

Table 1 M1 and M2 coordination numbers obtained from room and high temperature RMCProfile modelling. Values in parentheses give the standard deviations of each population calculated from 8 different starting configurations. Corresponding values for % are ~1%

	M1 sites				M2 sites	
CN	RT (count)	RT (%)	HT (count)	HT (%)	RT (count)	RT (%)
<4	1(1)	0	3(2)	0	0(1)	0
4	293(8)	20	382(7)	26	1(1)	1
5	633(20)	45	709(20)	47	4(1)	5
6	462(10)	33	387(20)	26	93(3)	89
>6	21(4)	2	16(3)	1	6(1)	5
Av.	5.149(7)		5.022(10)		6.00(3)	

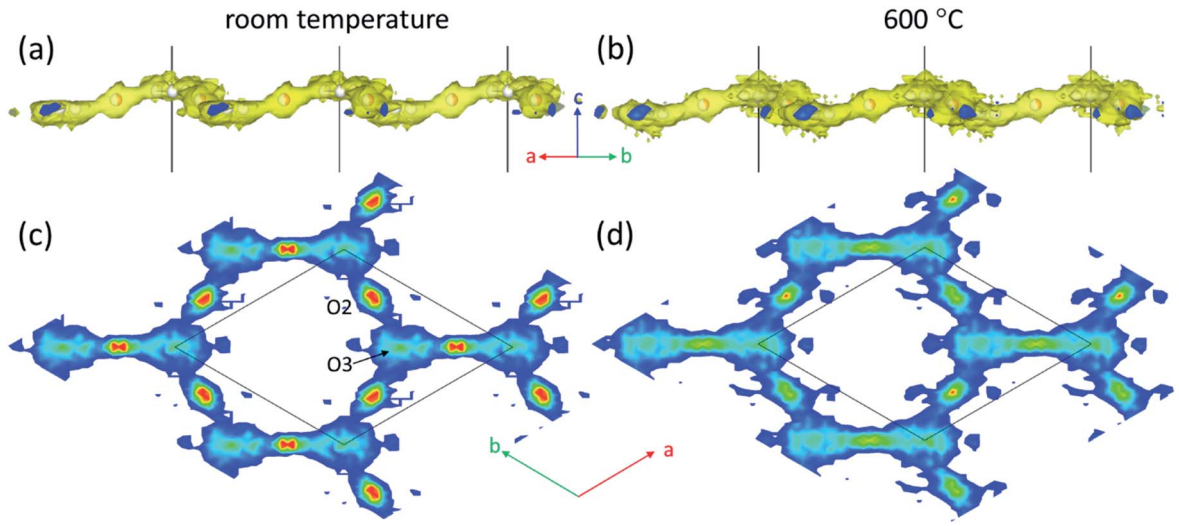

Fig. 6 Cloud plots encompassing volumes occupied by O2 and O3 atoms viewed down [110] at (a) room temperature and (b) 600 °C. (c and d) Show atomic density cross section of a single layer of O2/O3 sites down the c axis. In panels c and d the artificial blue-to-green-to-red colouring scheme used represents atomic densities from 1.5 (blue) to >96 (red) atoms per voxel.

Oxide ion conduction pathway

The most direct insight into the origin of high ionic conductivity in $Ba_3NbMoO_{8.5}$ comes from the cloud plots of oxygen atom distributions shown in Fig. 6. The yellow surfaces in Fig. 6a and b show the volume of space occupied by a single layer of O2 and O3 viewed perpendicular to the *c* axis at room temperature and 600 °C, respectively. The undulating nature of the volume relates to different positions of O2 and O3 along the *c* axis as shown in Fig. 1. Fig. 6c and d show contour plots of the atomic density viewed down the *c* axis, where the O2 and O3 atoms have been collapsed onto the same *z* coordinate. At room temperature we observe a distribution of oxygen positions, though O2 in particular is predominantly located close to the sites suggested by the average structure. In contrast, at 600 °C the distribution is significantly more diffuse and we observe an essentially continuous distribution of oxygen atoms around the hexagonal "rings" of Fig. 6f. The minor departure from full six-fold symmetry in both plots is caused by the shape of the simulation box used (it is eliminated using a tetragonal simulation box). The visual appearance of these rings is similar to the probability distribution implied by the size and shape of atomic displacement ellipsoids from single crystal refinements[12] and to the neutron scattering length density maps reported by maximum entropy methods.[24] Similar cloud plots for O1 and M1 (Fig. 4c) show the corresponding sites are significantly less broadly distributed. The PDF study therefore implies relatively facile diffusion of oxide ions in two dimensions in the *ab* plane, with any diffusion along the *c* direction occurring *via* a more conventional vacancy migration mechanism. A single crystal conductivity study would help confirm the anisotropic nature of this property.

Conclusions

In conclusion, we report X-ray and neutron powder diffraction and neutron total scattering/PDF studies which give important new insight into both the average and local structure of $Ba_3NbMoO_{8.5}$. Synchrotron X-ray experiments have shown a thermal-history-dependent phase transition occurs between ~150 and ~350 °C which helps explain unusual variation in the unit cell parameters found in earlier works. This transition is most likely associated with the redistribution of M atoms that occurs on heating. This process is likely to be rapid at the high (1100 °C) synthesis temperatures but significantly slower at lower temperature. Combined modelling of Bragg, $D(r)$ and $F(q)$ data from neutron scattering experiments gives a strong indication that $Ba_3NbMoO_{8.5}$ contains a mixture of 4, 5 and 6 coordinate M sites, with a preference for 5-fold coordination. The variable M coordination leads to a broad distribution of oxygen sites at room temperature, and a distribution which is essentially continuous in the *ab* plane at 600 °C. The continuous distribution could explain the reduction in activation energy for O migration previously reported at $T > 500$ °C. The change in O2/O3 distribution and its influence on M coordination presumably drives the redistribution over M1/M2 sites that occurs on heating.

There has been a recent suggestion that $Ba_3NbMoO_{8.5}$ loses oxygen at high temperature.[24] Our TGA data also suggest mass loss, and variable temperature Rietveld refinement indicates a possible decrease in the fractional occupancy of certain oxygen sites with temperature, though this depends on the model used. We do, however, find strong evidence for H_2O loss at ~400 °C by TGA-MS. This, combined with ^1H NMR observations suggests that water loss is more likely. This conclusion is consistent with earlier concentration cell and pO_2 measurements that show $Ba_3NbMoO_{8.5}$ is a predominantly oxide ion conductor (O transference 0.97–0.99 in air) and that there is no evidence of n-type conductivity until $pO_2 \lesssim 10^{-20}$ atm at 600 °C. Previous studies under moist air also showed no significant proton contribution to the conductivity. The bulk and grain boundary conductivity both decrease in moist air at temperatures below 600 °C, which

would suggest the incorporation of protons into the structure impedes oxide ion conductivity.[9]

In summary, we report the first detailed picture of the local structure of $Ba_3NbMoO_{8.5}$ using total scattering methods and we relate its high oxide ion conductivity to the facile two dimensional diffusion through O2/O3-derived sites in the *ab* plane.

Conflicts of interest

There are no conflicts to declare.

Acknowledgements

M. S. C. thanks Diamond Light Source and Durham University for a PhD studentship. I. R. E. acknowledges the Royal Society and the Leverhulme Trust for the award of a Senior Research Fellowship (SRF\R1\180040). J. E. A. acknowledges the support of a Newton International Fellowship (NF170809) awarded by The Royal Society. We thank Dr Sascha Fop for assistance with TGA-MS experiments and Dr David Apperley for recording the solid state NMR spectra. We gratefully acknowledge the Science and Technology Facilities Council (STFC) for access to neutron beamtime at POLARIS, ISIS (RB1810088), and thank Dr Helen Playford for assistance during the data collection. We acknowledge Diamond Light Source for time on Beamline I11 under Proposal EE19729 and thank Dr Sarah Day and Prof Chiu Tang for assistance during data collection.

Notes and references

1 D. Yuan and F. A. Kröger, *J. Electrochem. Soc.*, 1969, **116**, 594–600.
2 J. Sunarso, S. Baumann, J. M. Serra, W. A. Meulenberg, S. Liu, Y. S. Lin and J. C. Diniz da Costa, *J. Membr. Sci.*, 2008, **320**, 13–41.
3 P. N. Dyer, R. E. Richards, S. L. Russek and D. M. Taylor, *Solid State Ionics*, 2000, **134**, 21–33.
4 E. D. Wachsman and K. L. Duncan, *Ceria/bismuth oxide bilayered electrolytes for low temperature solid oxide fuel cells*, Electrochemical Society Inc, Pennington, 1999.
5 S. J. Skinner and J. A. Kilner, *Mater. Today*, 2003, **6**, 30–37.
6 D. J. L. Brett, A. Atkinson, N. P. Brandon and S. J. Skinner, *Chem. Soc. Rev.*, 2008, **37**, 1568–1578.
7 A. Bernasconi, C. Tealdi and L. Malavasi, *Inorg. Chem.*, 2018, **57**, 6746–6752.
8 A. Bernasconi, C. Tealdi, M. Mühlbauer and L. Malavasi, *J. Solid State Chem.*, 2018, **258**, 628–633.
9 S. Fop, J. M. S. Skakle, A. C. McLaughlin, P. A. Connor, J. T. S. Irvine, R. I. Smith and E. J. Wildman, *J. Am. Chem. Soc.*, 2016, **138**, 16764–16769.
10 S. Fop, E. J. Wildman, J. T. S. Irvine, P. A. Connor, J. M. S. Skakle, C. Ritter and A. C. McLaughlin, *Chem. Mater.*, 2017, **29**, 4146–4152.
11 S. Fop, E. J. Wildman, J. M. S. Skakle, C. Ritter and A. C. McLaughlin, *Inorg. Chem.*, 2017, **56**, 10505–10512.
12 J. E. Auckett, K. L. Milton and I. R. Evans, *Chem. Mater.*, 2019, **31**, 1715–1719.
13 L. Malavasi, H. Kim, S. J. L. Billinge, T. Proffen, C. Tealdi and G. Flor, *J. Am. Chem. Soc.*, 2007, **129**, 6903–6907.
14 A. Mancini, C. Tealdi and L. Malavasi, *Int. J. Hydrogen Energy*, 2012, **37**, 8073–8080.
15 S. T. Norberg, S. Hull, I. Ahmed, S. G. Eriksson, D. Marrocchelli, P. A. Madden, P. Li and J. T. S. Irvine, *Chem. Mater.*, 2011, **23**, 1356–1364.
16 M. Project, https://www.mantidproject.org/Main_Page, accessed 11/04/2019, 2019.
17 A. A. Coelho, J. S. O. Evans, I. R. Evans, A. Kern and S. Parsons, *Powder Diffr.*, 2011, **26**, S22.
18 H. M. Rietveld, *J. Appl. Crystallogr.*, 1969, **2**, 65–71.
19 A. K. Soper, 2012, programs for correcting raw neutron and X-ray total scattering data to differential cross section.
20 A. A. Coelho, P. A. Chater and A. Kern, *J. Appl. Crystallogr.*, 2015, **48**, 869–875.
21 D. A. Keen, *J. Appl. Crystallogr.*, 2001, **34**, 172–177.
22 M. G. Tucker, D. A. Keen, M. T. Dove, A. L. Goodwin and Q. Hui, *J. Phys.: Condens. Matter*, 2007, **19**, 335218.
23 K. Momma and F. Izumi, *J. Appl. Crystallogr.*, 2011, **44**, 1272–1276.
24 M. Yashima, T. Tsujiguchi, K. Fujii, E. Niwa, S. Nishioka, J. R. Hester and K. Maeda, *J. Mater. Chem. A*, 2019, **7**, 13910.
25 R. Hill, *J. Appl. Crystallogr.*, 1992, **25**, 589–610.
26 S. Corallini, M. Ceretti, A. Cousson, C. Ritter, M. Longhin, P. Papet and W. Paulus, *Inorganic chemistry*, 2017, **56**, 2977–2984.
27 M. T. Dunstan, F. Blanc, M. Avdeev, G. J. McIntyre, C. P. Grey and C. D. Ling, *Chem. Mater.*, 2013, **25**, 3154–3161.
28 I. R. Evans, J. A. K. Howard and J. S. O. Evans, *Chem. Mater.*, 2005, **17**, 4074–4077.
29 J. R. Peet, C. A. Fuller, B. Frick, M. Zbiri, A. Piovano, M. R. Johnson and I. R. Evans, *Chem. Mater.*, 2017, **29**, 3020–3028.
30 M. L. Tate, J. Hack, X. J. Kuang, G. J. McIntyre, R. L. Withers, M. R. Johnson and I. R. Evans, *J. Solid State Chem.*, 2015, **225**, 383–390.
31 K. S. McCombie, E. J. Wildman, S. Fop, R. I. Smith, J. M. S. Skakle and A. C. McLaughlin, *J. Mater. Chem. A*, 2018, **6**, 5290–5295.
32 K. S. McCombie, E. J. Wildman, C. Ritter, R. I. Smith, J. M. S. Skakle and A. C. McLaughlin, *Inorganic Chemistry*, 2018, **57**, 11942–11947.
33 A. W. Addison, T. N. Rao, J. Reedijk, J. van Rijn and G. C. Verschoor, *J. Chem. Soc., Dalton Trans.*, 1984, 1349–1356, DOI: 10.1039/dt9840001349.
34 D. Waroquiers, X. Gonze, G. M. Rignanese, C. Welker-Nieuwoudt, F. Rosowski, M. Göbel, S. Schenk, P. Degelmann, R. André, R. Glaum and G. Hautier, *Chem. Mater.*, 2017, **29**, 8346–8360.
35 F. D. Hardcastle and I. E. Wachs, *J. Raman Spectrosc.*, 1990, **21**, 683–691.
36 F. D. Hardcastle and I. E. Wachs, *J. Phys. Chem.*, 1991, **95**, 10763–10772.
37 V. I. Tsaryuk and V. F. Zolin, *Spectrochim. Acta, Part A*, 2001, **57**, 355–359.

